The interaction between ion transit-time and electron drift instabilities and their effect on anomalous electron transport in Hall thrusters

Thomas Charoy, Trevor Lafleur, Alejandro Alvarez-Laguna, Anne Bourdon, Pascal Chabert

The interaction between ion transit-time and electron drift instabilities and their effect on anomalous electron transport in Hall thrusters

To cite this article before publication: Thomas Charoy *et al* 2021 *Plasma Sources Sci. Technol.* in press https://doi.org/10.1088/1361-6595/ac02b3

The interaction between ion transit-time and electron drift instabilities and their effect on anomalous electron transport in Hall thrusters

T. Charoy[1], T. Lafleur[2], A. Alvarez Laguna[1], A. Bourdon[1], P. Chabert[1]

[1] *Laboratoire de Physique des Plasmas (LPP), CNRS, Sorbonne Université, École polytechnique, Institut Polytechnique de Paris, 91120 Palaiseau, France.*
[2] *PlasmaPotential-Physics Consulting and Research, Canberra, ACT 2601, Australia*

E-mail: thomas.charoy@lpp.polytechnique.fr

October 2020

Abstract. Recent simulations and experiments have observed a transition from short to long-wavelength azimuthal instabilities that leads to enhanced electron transport in Hall thrusters. Here we make the hypothesis that this phenomenon stems directly from the interaction between the axial Ion Transit-Time Instability (ITTI), and the azimuthal Electron Drift Instability (EDI). This interaction is studied using 2D axial-azimuthal self-consistent Particle-in-Cell simulations which include a 1D neutral dynamics solver. It is found that a short to long-wavelength transition only occurs if the Breathing-Mode (BM) and ITTI are captured in the simulation, and two distinct instability regions can be distinguished depending on the local ion Mach number. Upstream of the ion sonic point the EDI exhibits an ion-acoustic behaviour, and the associated instability-enhanced electron transport is well described by a previously developed model based on kinetic theory. Downstream of the ion sonic point however, the ITTI significantly changes the local plasma parameters, and this modifies the EDI while increasing the electron transport.

Keywords: Hall thrusters, particle-in-cell, electron drift instability, transport, ion transit-time instability

Submitted to: *Plasma Sources Sci. Technol.*

1. Introduction

Due to their high specific impulse, electric thrusters are increasingly being used for various space missions [1, 2]. The Hall thruster (HT) is currently one of the most

successful and widespread systems because of its efficiency and relatively high thrust-to-power ratio [3]. In these devices, a propellant injected at the base (anode) of an annular channel is ionized by electrons emitted at the opposite end from an external hollow cathode. The potential difference imposed between the anode and the cathode induces an axial electric field $\mathbf{E}$ which accelerates newly formed ions out of the channel to produce thrust. A radial magnetic field $\mathbf{B}$ is applied to limit the axial motion of the electrons (causing them to drift in the azimuthal $\mathbf{E} \times \mathbf{B}$ direction) and increase their residence time to enhance ionization. Despite the apparent simplicity of their operation, many aspects of HT physics are not fully understood. Consequently, thruster design still involves a significant empirical aspect that can limit efficiency, and increase development times and costs. To address the widening need of thruster capabilities (size, power, lifetime, etc.) for diverse applications, predictive numerical models are needed for a deeper understanding, and to better aid the design process.

More specifically, axial electron transport needs to be self-consistently accounted for to correctly capture the complete discharge behaviour. Even though it has been known for decades that classical electron-neutral or electron-ion collisions are not sufficient to explain experimentally observed electron mobilities [4], the origin of this so-called *anomalous transport* is still not understood. Plasma/wall interactions were initially thought to be the major contributor to this anomalous transport [3], through near-wall conductivity enhanced by secondary electron emission [5, 6] or radial sheath instabilities [7, 8]. But while it is undeniable that the walls play a role on the electron transport, it is generally much lower [9, 10, 11] than that produced by the Electron Drift Instability (EDI) [12, 13], which is a kinetic instability propagating in the azimuthal direction. The large azimuthal electron drift velocity in HTs drives a strong kinetic streaming instability that has been confirmed and studied in a number of works [14, 15, 16, 17, 18, 19, 20], and Lafleur *et al.* [21, 22] have highlighted the crucial role of these azimuthal instabilities in enhancing electron scattering. The instability is characterised by short-wavelength, high-frequency, oscillations that lead to an instability-enhanced electron-ion friction force that can be orders of magnitude higher than that due to classical electron-ion Coulomb collisions alone [20].

A theoretical model based on kinetic theory has been developed [23, 24] to approximate this instability-enhanced friction force (and hence self-consistently account for anomalous electron transport from first principles). However, recent numerical simulations accounting for the HT azimuthal direction, both fluid [25] and Particle-in-Cell (PIC) [26, 27, 28, 29], have observed a change in short-wavelength EDI modes towards larger wavelength azimuthal structures via a so-called inverse energy cascade. These observations have been supported by experimental measurements with ion saturation probes [30] in which the wave energy was found to be convected by low-frequency azimuthal oscillations in the plume. Such low-frequency, long-wavelength, oscillations are not present in PIC simulations with a short azimuthal domain length (around 1 cm; which precludes the formation of large azimuthal structures), and are not described by the kinetic model.

A mode transition towards larger wavelength azimuthal structures has not yet been observed in simulation codes that include the axial HT direction, which would allow the azimuthal wave to be convected downstream, and be presumably strongly influenced by any axial instabilities [25]. The low-frequency (1-20 kHz) breathing mode (BM) and, to a lesser extent medium-frequency (100-500 kHz) ion transit-time instabilities (ITTI), can induce a strong variation in local plasma parameters, and hence would be expected to impact the growth and saturation of the EDI. A preliminary study was performed by Powis *et al.* [31] by increasing the azimuthal domain length of a simplified axial-azimuthal benchmark case [32] and no large structures or inverse cascades were observed. However, due to an imposed ionization source term, no axial instabilities were generated, and EDI wave convection was only present in an otherwise "stable" plasma. It is thus important to include neutral dynamics (hence accounting self-consistently for the ionization) to fully capture the BM and ITTI, investigate how they interact with the EDI, and determine whether this affects anomalous electron transport.

Self-consistent, axial-azimuthal, simulations have been performed with *LPPic*, a massively parallelized 2D PIC code, extensively verified in [33, 32]. However, for a PIC code to be stable, the numerical parameters (time step Δt and cell size Δx) need to resolve the electron plasma frequency ω_{pe} and the Debye length λ_d [34] respectively:

$$\begin{cases} \Delta t \leq \dfrac{0.2}{\omega_{pe}} = 0.2\sqrt{\dfrac{m\epsilon_0}{n_e q^2}} \\ \Delta x \leq \lambda_d = \sqrt{\dfrac{\epsilon_0 k_B T_e}{n_e q^2}} \end{cases} \tag{1}$$

with k_B Boltzmann's constant, ϵ_0 the vacuum permittivity, and T_e the electron temperature. Due to the BM oscillations, the electron density can reach relatively high values ($n_e \approx$ 2-3 $\times$ 10^{18} m^{-3}) and hence, very small numerical parameters need to be used ($\Delta x \approx 2 \times 10^{-5}$ m, $\Delta t \approx 2 \times 10^{-12}$ s). Moreover, to capture several low-frequency BM oscillations, at least 150 μs need to be simulated, which increases significantly the computational time. Whereas an implicit scheme for the electron motion can be used [15], it can induce artificial electron cooling when a magnetic field is included [35]. Hence, to speed-up computations, we increase the vacuum permittivity in this study by a factor of α_ϵ (i.e. $\epsilon_0^* = \alpha_\epsilon \epsilon_0$), similar to that used in [16]. According to equation 1, the time step and cell size can then be increased by a corresponding factor of $\sqrt{\alpha_\epsilon}$ (while keeping the same axial and azimuthal length) which reduces significantly the computational time. However, the EDI growth rate depends on the vacuum permittivity and hence such a scaling technique tends to damp the instability (this will be discussed further in section 4 below).

In this work, we first show in section 2 that without any axial instabilities (i.e. the BM and ITTI), there is no mode transition towards larger wavelength azimuthal structures and the kinetic model of Eq. 2 describes very well the anomalous electron transport. Then, after a brief description of the self-consistent PIC model (which now allows the formation of the BM and ITTI), the azimuthal domain length is

increased in section 3 and we show that long wavelength structures appear and propagate azimuthally. Finally, in section 4 we show that the transition from short-wavelength, high-frequency, modes to long-wavelength, low-frequency, modes stems from an interaction between the azimuthal EDI and the axial ITTI, and we discuss how this affects the resulting electron transport.

2. Steady non self-consistent simulations

In this section, a simplified axial-azimuthal PIC simulation is used, with a 2D Cartesian mesh with an axial length of $L_x = 2.5$ cm, and an azimuthal length of $L_y = 1.28$ cm. The radial magnetic field profile is imposed, with a maximum at $x = 0.75$ cm, and no collisions or neutral dynamics are considered: ionization is accounted non self-consistently for by imposing a source term with a cosine profile, hence precluding the formation of any axial instabilities. As this simulation case has been extensively used and described previously in [36, 32, 37], and used as a benchmark between 7 independent codes [32], no additional details are given here for brevity.

2.1. Theoretical model for the electron-ion friction force

The above PIC simulation model was recently used [24] to stress-test the model developed by Lafleur *et al.* [23] within the context of HTs to approximate the instability-enhanced electron-ion friction force. Further details can be found in these references, but we highlight three important approximations used:

- Quasi-linear theory is valid (i.e. plasma potential fluctuations are much smaller than the electron temperature, $\frac{\langle \delta\phi \rangle}{T_e} \ll 1$),
- The instability propagates in the azimuthal direction with a single dominant wave number k_y,
- Electron cyclotron resonances are smeared out and the instability exhibits an ion-acoustic behaviour (i.e. $k_y\lambda_d = \frac{1}{\sqrt{2}}$, with the phase velocity $v_\phi \approx c_s \ll v_{e,y}$, and $c_s = \sqrt{\frac{k_B T_e}{M}}$ the ion sound speed, with M the ion mass).

With the above approximations, an expression for the instability-enhanced friction force can be obtained

$$R_{ei,approx} = 2\sqrt{2}\pi\omega_{pe}^2\lambda_d\epsilon_{wave}\left.\frac{dF_{e0}}{dv_y}\right|_{v_y=0} \tag{2}$$

with $\epsilon_{wave} = \frac{1}{2}\epsilon_0\langle|\delta\mathbf{E}|\rangle_{rms}^2 = \frac{1}{4}\epsilon_0|\delta\mathbf{E}|^2$ the energy density of the wave electric field, and F_{e0} the equilibrium (i.e. time and space-averaged over the instability frequency and wavelength) normalized Electron Velocity Distribution Function (EVDF).

It is worth mentioning that in section 4.2 we will relax the third approximation listed above, and will instead obtain a more accurate dominant wavenumber directly from the simulations by making use of a Fast Fourier Transform (FFT) instead of using the ion-acoustic approximation $k_y\lambda_d = \frac{1}{\sqrt{2}}$.

2.2. Increase of azimuthal domain length

It was found in [24] that the anomalous electron transport is dominated by an instability-enhanced friction force, and that this force is very well described by $R_{ei,approx}$ in equation 2 for multiple configuration cases (with different magnetic fields and discharge currents). However, the imposed azimuthal domain length was relatively short and hence, no long-wavelength azimuthal instabilities were present. Here we remove this limitation, and significantly increase the azimuthal domain length to 10.24 cm, but keep the same cell size (i.e. the number of azimuthal simulation grid points increases by a factor of 8). 2D snapshots of the azimuthal electric field at steady-state are displayed in figure 1, along with the corresponding 2D FFT (performed over a simulation duration of 10 μs) at two axial positions. We can see that no long-wavelength structures are present (similar to the results of Powis *et al.* [31]) and that the azimuthal instability has a dominant wavelength close to that predicted by the modified ion-acoustic dispersion relation [22, 20]

$$\omega_R \approx \mathbf{k}.\mathbf{v}_{di} \pm \frac{kc_s}{\sqrt{1+k^2\lambda_d^2}}, \tag{3}$$

$$\gamma \approx \pm\sqrt{\frac{\pi m}{8M}}\frac{\mathbf{k}.\mathbf{v}_{de}}{(1+k^2\lambda_d^2)^{3/2}}\,, \tag{4}$$

with $\mathbf{v}_{de}$ and $\mathbf{v}_{di}$ the azimuthal electron and ion drift velocities respectively.

Although the modified ion-acoustic dispersion relation (DR) fits perfectly with the wave spectrum inside the thruster, this is not the case in the plume. Following previous works [30, 38], the wave spectrum in this region was overlapped with the modified ion-acoustic DR based instead on the plasma parameters in the upstream region (at an axial position $x = 0.5$ cm, which corresponds approximately to the origin of the EDI and the maximum plasma density). The good agreement obtained with this shifted DR shows that the EDI is convected downstream, and that it maintains some of its characteristics (in this case the wave phase velocity). We have also verified that for the benchmark results presented in [32] (where $L_y = 1.28$ cm), the shifted modified DR also fits well with the PIC wave spectrum in the plume. Additionally, in the new simulations presented here, it was observed that the separation between the two instability zones seen in figure 1 not only corresponds to the location of the maximum magnetic field, but also the ion sonic point (i.e. the location where the axial ion velocity v_{ix} has reached the ion sound speed c_s; not shown in figure 1 as it overlaps almost perfectly).

With the results above, we have shown that no long-wavelength structures appear in the simplified benchmark case, despite the use of a significantly longer azimuthal domain length. Figure 2 shows the electron-ion friction force obtained from the PIC simulations (found from $R_{ei} = q\langle\delta n_e \delta E_y\rangle$ with δn_e and δE_y oscillations about the equilibrium values of the electron density and azimuthal electric field respectively; see [22, 19]), together with that predicted from kinetic theory (Eq. 2). As can be seen, kinetic theory is generally in good agreement with the PIC results, and describes quite well the instability-enhanced friction force. Although the PIC simulation model is simplified and

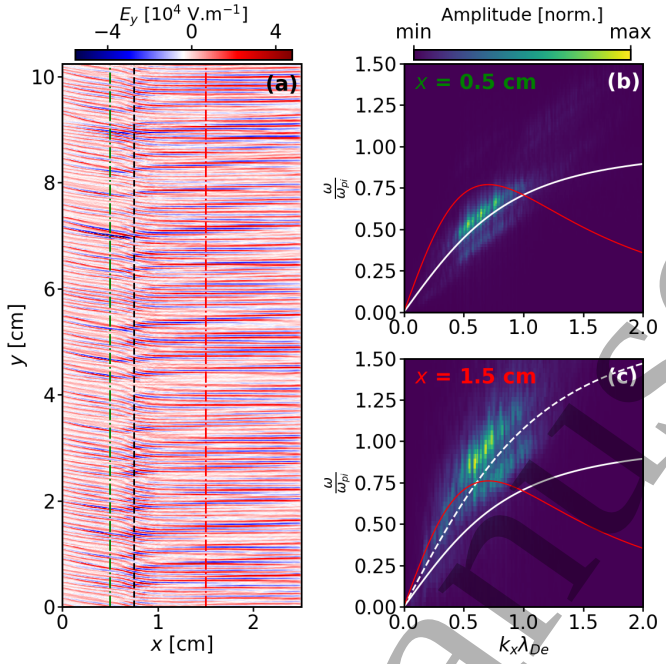

Figure 1: **Simplified benchmark case with L_y=10.24 cm**: (a) 2D map of the azimuthal electric field. The green and red vertical dashed lines indicate the position of the FFT. The black vertical dashed line corresponds to the position of the maximum magnetic field and the ion sonic point respectively. (b) 2D FFT at x=0.5 cm. (c) 2D FFT at x=1.5 cm. White thick line: local ion-acoustic dispersion relation. White dashed line: ion-acoustic dispersion relation (Eq. 3) convected from x=0.5 cm. Red dashed line: ion-acoustic growth rate (Eq. 4) rescaled by a constant factor to fit the image. The spectrum has been zoomed to focus on the zone of interest.

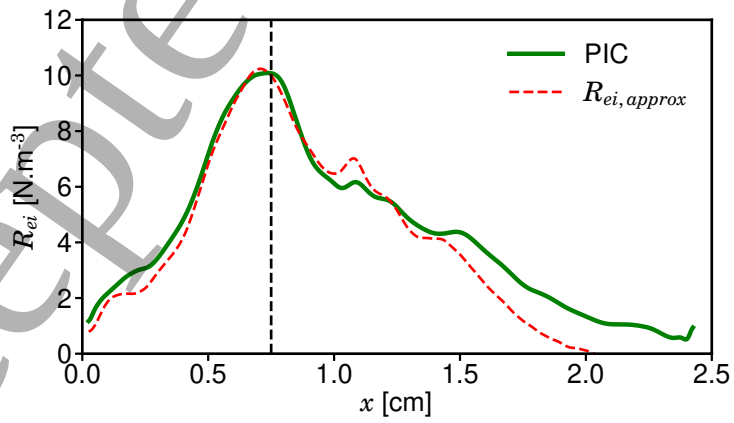

Figure 2: **Simplified benchmark case with L_y=10.24 cm**: Comparison of the friction force obtained directly from the PIC (green) with that predicted by the kinetic model in Eq. 2 (red).

has a number of limitations, these results still give important insight into the behaviour of the azimuthal instabilities in 2D axial-azimuthal simulations: in the absence of the BM or ITTI, there is no mode transition towards long-wavelength, low-frequency waves.

3. Self-consistent simulations

We have seen in the previous section that large-wavelength azimuthal waves are not observed in a 2D axial-azimuthal PIC simulation if ionization is artificially imposed and neutral dynamics ignored. Here, we remove this limitation by solving for the neutral dynamics and accounting for ionization self-consistently with a Monte Carlo Collision (MCC) module.

3.1. Description of the model

The axial-azimuthal (x-y) simulation domain is similar to that used in [16, 19], with a 2D Cartesian mesh shown in figure 3(a). The HT channel length is 2.5 cm, and the simulation domain includes a plume length of 1.5 cm, which gives a total axial domain length of $L_x = 4$ cm. The imposed potential at the anode ($x = 0$ cm) is 300 V while the cathode ($x = L_x = 4$ cm) is grounded (0 V). Whereas only a small part of the HT azimuthal direction is usually simulated ($L_y = 1$ cm) to speed-up the simulations, L_y is increased in this section, with imposed periodic azimuthal boundary conditions. The axial profile of the imposed radial magnetic field is displayed in figure 3(b) and the position of its maximum corresponds to the exit plane of the thruster.

In contrast to the simplified benchmark case in section 2, electron-neutral and ion-neutral collisions are now taken into account through a MCC module (as described in [33]) and ionization is calculated self-consistently. The xenon neutral gas is considered as a fluid and azimuthal gradients are neglected. Hence, the 1D Euler equations are:

$$\begin{cases} \partial_t \rho_g + \partial_x(\rho_g u_g) = S_1 \\ \partial_t(\rho_g u_g) + \partial_x(\rho_g u_g^2) = -\partial_x P_g + S_2 \\ \partial_t E_g + \partial_x(E_g u_g) = -\partial_x(P_g u_g) - \dfrac{E_g - E_g'}{\tau} \end{cases} \tag{5}$$

with S_1 and S_2 collisional source terms, ρ_g, u_g, P_g, E_g respectively the neutral density, velocity, pressure and energy density given by

$$E_g = \frac{P_g}{\gamma - 1} + \frac{1}{2}\rho_g u_g^2, \tag{6}$$

with γ the ratio of specific heats. Only the effect of ionization has been taken into account in the source terms S_1 and S_2: i.e. $S_1 = -\rho_g S_{iz}$ and $S_2 = -\rho_g u_g S_{iz}$ with S_{iz} the ionization rate computed every time step from the MCC module and averaged in the azimuthal direction. The source term $\frac{E_g - E_g'}{\tau}$ for the energy equation includes a parameter τ that is set in order to make the energy density E_g converge to an imposed value E_g' corresponding to a constant temperature of $T_g = 640$ K. One can notice that imposing

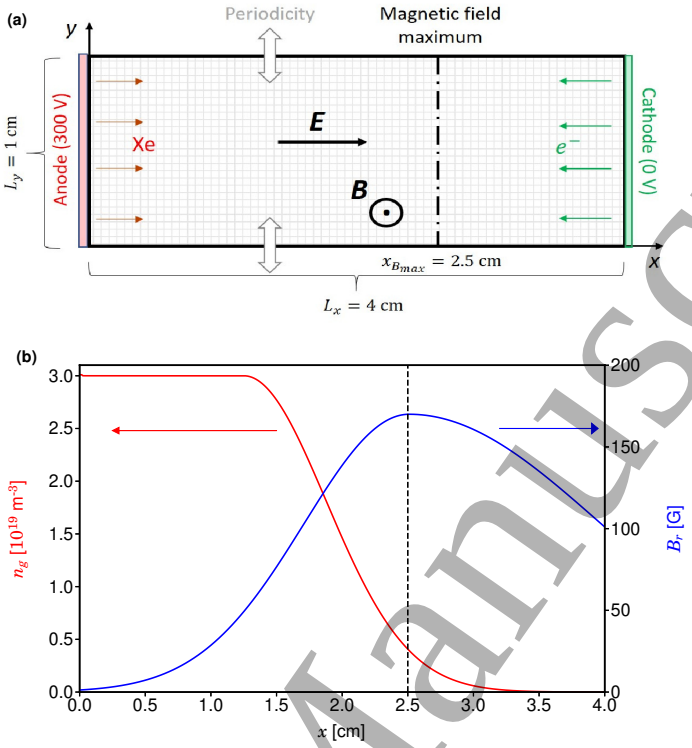

Figure 3: (a) Simulation domain with x the axial direction, and y the (periodic) azimuthal direction. Black dot-dashed line ($x_{B_{max}}$=2.5 cm): position of the maximum radial magnetic field strength. Xenon atoms are injected at the anode and electrons are emitted from the cathode. (b) Axial profiles of the imposed radial magnetic field and initial neutral density. The dashed line corresponds to the position of the maximum radial magnetic field.

this neutral temperature makes the system isothermal, and hence the energy equation becomes redundant. However, it has been included to help numerical convergence, and to more easily account for any energy sources or losses in future work. Equation 5 are solved with a HLLC Riemann solver [39]. The initial neutral density axial profile is displayed in figure 3(b) and the initial neutral velocity is considered uniform and equal to 200 m·s^{-1}. The neutral mass flow rate at the anode is fixed at $\dot{m}$ = 5 mg·s^{-1} and ions lost at the anode recombine and reappear as neutral atoms. This recombination has been directly included in the anode boundary condition and more details on its implementation can be found in [40]. These parameters, along with the radial magnetic field profile, are similar to those used by Lafleur *et al* [19] in which only the neutral continuity equation was solved (without ion recombination at the anode) and a constant axial velocity of the neutral gas assumed. The main drawback of not considering the azimuthal direction for the neutral dynamics is related to rotating spokes that may originate from an azimuthal variation of neutral density [41] and hence, cannot be captured in our simulations.

Because of BM oscillations, the plasma density can vary by a factor of almost 5 (from $n_e \approx 5 \times 10^{17}$ m^{-3} to $n_e \approx 2.5 \times 10^{18}$ m^{-3}). When the plasma density is a maximum, the electron temperature is around 20 eV. Hence, to comply with the PIC stability criteria in equations 1, the time step Δt and the cell size Δx have been fixed to 2×10^{-12} s and 2×10^{-5} m, respectively. This gives a computational mesh of N_x=2000 cells in the axial direction and N_y=512 cells in the azimuthal direction. At initialisation, the particles are loaded uniformly with a density of $n_{p,ini}$= 10^{18} m^{-3} and the initial number of macroparticles per cell has been fixed at 400 to reduce numerical noise. As the BM frequency is around 20 kHz, simulation cases have been run for at least 150 μs to capture several BM periods.

Electron injection at the cathode needed to sustain the discharge is treated differently to that used previously in [16, 36, 32], in which current balance considered. As already mentioned in previous works [42, 19], this cathode model appears to create a cathode sheath and violate current conservation during any transient state, which can be a challenge when accounting for axial instabilities. Hence, electrons are injected according to a quasi-neutral assumption: at each time step, the charge difference between ions and electrons at the right domain boundary (cathode) is calculated and if this charge difference is positive, the corresponding number of electrons is injected uniformly to compensate. If the charge difference is negative, no electrons are emitted.

Even though the *LPPic* code has been extensively parallelized with MPI, using a domain decomposition coupled with dynamic load balancing, the computational cost is still too heavy and, as described above in section 1, we need to artificially increase the vacuum permittivity ϵ_0 by a factor α_ϵ. The influence of this scaling technique will be studied in section 4.1 by varying the scaling factor α_ϵ from 4 to 256. Despite this scaling technique, the simulation cases remain very computationally expensive, as seen in table 1 (to ease the comparison, the computational times correspond to the first 150 μs of simulation, but often, longer times have been simulated to be able to capture steady BM oscillations).

Case	$\boldsymbol{\alpha_\epsilon}$	$\boldsymbol{L_y}$ **(cm)**	$\boldsymbol{N_{CPU}}$	**Time (days)**	**CPU hours (k)**	$\boldsymbol{N_{part,max}}$	**Simulated time ([μs])**
1	4	1	1260	60	1800	2×10^8	150
2	16	1	840	7	140	6×10^7	250
3	64	1	360	5	45	1×10^7	300
4	256	1	96	1	2.3	3×10^6	300
5	64	2	700	5	90	2×10^7	350
6	64	4	1120	9	240	1×10^8	350
7	64	8	1680	12	480	3×10^8	350

Table 1: Typical computational requirements for the self-consistent simulations (the given time and CPU hours corresponds to the cost for 150 μs of simulation time). The total simulated time is indicated in the last column.

Currently, simulating the real case with $\alpha_\epsilon = 1$ would require both a very long time (around 1 year on 1500 CPUs) and a large CPU memory (to store around 10^9 macroparticles), which is currently not possible. To speed-up the computation and at the same time reduce the number of macroparticles, a merging-splitting algorithm could be used to make the number of particles per cell constant independent of the simulation time and position. However, such an algorithm can impact the electron distribution function, and hence affect the electron transport [19, 24]. We therefore choose not to use any merging-splitting algorithm.

3.2. Variation of azimuthal domain length

To investigate mode transitions and possible inverse energy cascades, the azimuthal domain length L_y has been increased from 1 cm to 2, 4 and 8 cm. As the computational burden is directly proportional to L_y, we have used a scaling factor of $\alpha_\epsilon = 64$. The time evolution of the discharge current, I_d, is displayed in figure 4(a). Here we see that for all cases, the axial BM oscillation is present, with a frequency of around 20 kHz. The BM oscillation amplitude is greatly enhanced when L_y is increased, while the time-averaged discharge current also increases.

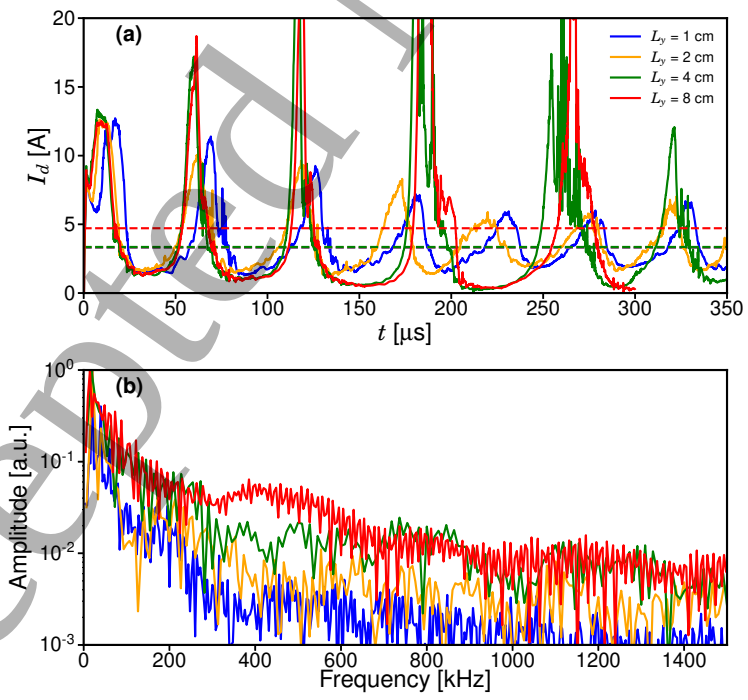

Figure 4: $\boldsymbol{\alpha_\epsilon = 64}$: For 4 values of azimuthal length L_y, (a) Time evolution of the discharge current and (b) Corresponding FFT. The dashed horizontal lines in (a) correspond to the mean value at equilibrium.

We also observe in figure 4(a) that an additional higher frequency mode is present, particularly during the falling part of each BM oscillation. A FFT has been performed on the discharge current and shown in figure 4(b). Along with the low-frequency BM peak, we found another spectral content at around 300-400 kHz, which is more important for longer azimuthal domain length L_y. This could be evidence of medium-frequency (100-500 kHz) ion transit-time instabilities (ITTI), observed experimentally [43, 44, 45], numerically [46, 47, 48, 16] and studied theoretically [49, 50, 51, 52, 53]. They are related to an instability associated with the transit of ions through the acceleration region. The axial electric field E_x includes a time-varying component that starts just downstream of the anode and propagates towards the cathode. This electric field creates a group of low-energy ions in the plume, along with some high-energy ions with an energy above that of the nominal anode-cathode potential (gained through wave-particle interactions).

The presence of the ITTI can also be inferred from the axial ion phase-space and the axial profile of the axial electric field, which are both displayed in figure 5(c,d) at two representative times for the case $L_y = 1$ cm (the case α_ϵ=16 will be discussed later in section 4.1). First, we can notice that a low-velocity ion group is present in the plume. Its origin can be understood by looking at the axial electric field in figure 5(c) which shows an axially propagating wave. The electric field trough is associated with a peak in the ion density (also seen in the phase space). These ions are partially trapped by the wave and are no longer accelerated by the nominal applied electric field, but instead are only convected at their initial velocity and form the low-velocity ion group in the plume.

The origin of the axial electric field wave appears to correspond to the ion sonic point. Moreover, one can notice that while this wave partially traps some ions, it also accelerates others to a velocity higher than $v_{i,max} = \sqrt{\frac{2|q|(U_d)}{m_e}}$, the velocity expected by the nominal applied potential difference U_d. Finally, it is important to mention that even though its amplitude is stronger when the discharge current decreases, we observe that the ITTI is also present when the discharge current increases; contrary to what was observed by Coche and Garrigues [16].

Fernandez *et al.* have derived a theoretical dispersion relation for the ITTI and they obtained, with the inclusion of electron pressure effects, the following simplified expression [52]:

$$\omega_{ITTI} \approx k_{ITTI}(v_{i0} \pm c_s). \tag{7}$$

Because the ITTI wavelength is of the order of the axial domain length, we cannot obtain a high-resolution dispersion relation from the PIC code. However, we have computed the theoretical frequency from Eq. 7, using the ion axial velocity v_{i0} and the ion sound speed c_s near the maximum growth rate (i.e. at the location of the minimum electron mobility). With a wavenumber between 200-400 m^{-1} (which gives a wavelength of the order of the discharge channel length), Eq. 7 gives a frequency ω_{ITTI} between 300-600 kHz for the case $L_y = 8$ cm, which is close to the value obtained in figure 4(b). Thus, the observed axial instability in the simulations appears consistent with the ITTI.

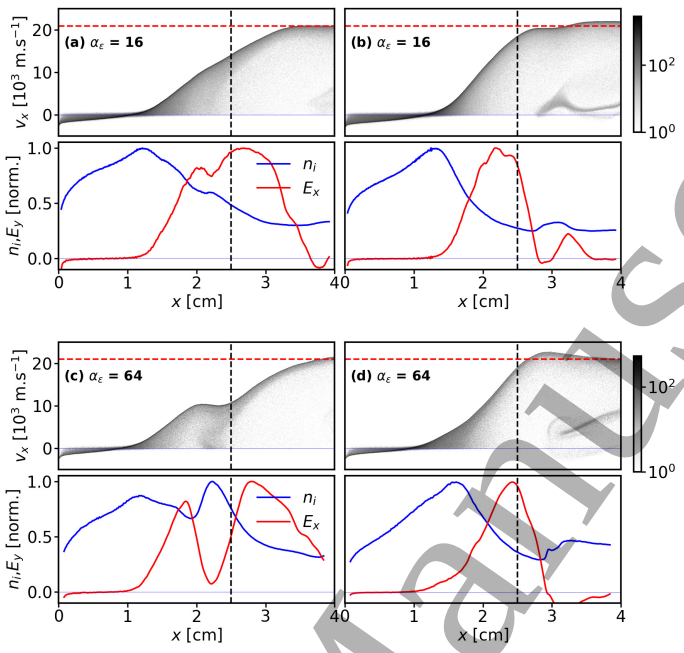

Figure 5: ***L_y*=1 cm**: Two representative times of an ion transit-time oscillation for two simulations with (a,b) α_ϵ=16 or (c,d) α_ϵ=64. Top: Axial ion phase-space with $v_{i,max}$ given by the horizontal red dashed line. Bottom: Corresponding normalized profiles of the ion density (blue line) and axial electric field (red line). The vertical dashed black line shows the position of the maximum magnetic field.

Having identified the presence of the BM and ITTI instabilities, we can check for any mode transition for a long azimuthal length. To this end, we have computed the Power Spectral Density (PSD) for the azimuthal electric field (with the function signal.welch from the *scipy* package [54]), and the normalized azimuthal wavenumber, $\frac{k_y L_y}{2\pi}$, is displayed as a function of the simulation time in figure 6 for different axial positions, and for the case $L_y = 8$ cm. Upstream of the ion sonic point ($x = 1$ cm; figure 6(a)), a continuous wavenumber spectrum is observed. However, downstream of the ion sonic point ($x = 2$ cm and $x = 3$ cm; figures 6(b,c)), we can see that the dominant wavenumber is higher when the discharge current rises (to the left of the vertical white dashed lines), but when the discharge current falls, it decreases sharply. This clearly shows that when the discharge current is a maximum, there is a transition from short-to-long wavelengths modes. Moreover, one can notice that downstream of the ion sonic point, a periodic structure with a frequency on the order of 300 kHz, can be identified, with a change of the dominant wavelength. This feature can be clearly seen near 160 μs, which shows again that the ITTI is also interacting with the EDI when the discharge current rises. A similar low frequency modulation of the EDI was recently observed

experimentally in a high-power pulsed magnetron (HIPIMS) discharge [55].

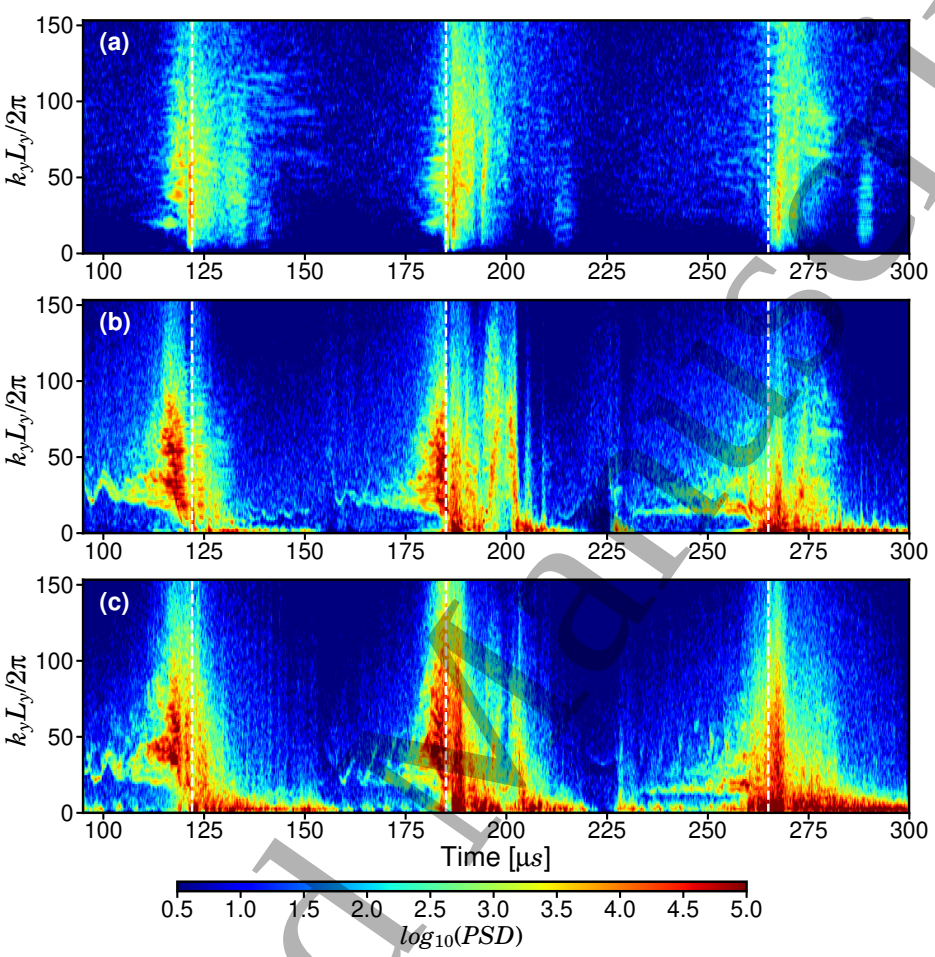

Figure 6: $\boldsymbol{\alpha_\epsilon = 64,\ L_y = 8\ cm}$: Power Spectral Density of the azimuthal electric field at (a) $x = 1$ cm, (b) $x = 2$ cm and (c) $x = 3$ cm. The white vertical dashed lines indicate the times when the discharge current is a maximum.

Despite the azimuthal electric field having a zero time-averaged value, there is a non-zero time-averaged correlation term, $R_{anom} = q\langle \delta n_e \delta E_y \rangle$, which we call here an "anomalous force". This anomalous azimuthal force (averaged over several BM and ITTI oscillations) is plotted in figure 7(a). In previous works [22, 20, 19, 24], and in section 2, this anomalous force was identified as an instability-enhanced electron-ion friction force. This is because the EDI significantly changes the screening of the Coulomb potential compared with that in a stable plasma, and extends the range over which electron-ion collisions can occur. In the present case, because of the ITTI (which is thought to be a fluid instability) and the long wavelength modes (which are much higher than the Debye length), it is no longer clear that the anomalous force is a friction. Regardless though, by comparing different terms in the electron momentum balance equation using the methods presented previously in [19, 24], the anomalous force term is still found to be the dominant contributor to the axial electron transport.

In figure 7(a), we can distinguish two axial zones: upstream of the ion sonic point, the anomalous force is low, whereas downstream of the ion sonic point, we observe a significant change as L_y is increased (particularly for the cases $L_y = 4$ and 8 cm), which enhances the axial transport. This helps to explain the discharge current behaviour in figure 4(a): a higher time-averaged current is associated with higher azimuthal domain lengths because the electron conductivity is enhanced by the anomalous force. This force increase is related to a significant increase of the wave energy density, ϵ_{wave}, downstream of the ion sonic point, as seen in figure 7(b). This can be explained by the mode transition observed: more energy is now carried by long-wavelength structures. This hypothesis is confirmed by applying a high-pass filter (5^{th} order filter with a cut-off frequency of 500 kHz, which is above the observed ITTI frequency) on the azimuthal electric field, hence allowing the wave energy density associated with just the high-frequency EDI fluctuations to be isolated. Figure 7(b) shows that the wave energy density is significantly lower if the effect of the low-frequency ITTI is removed.

Overall, in contrast to the non self-consistent simulations in section 2, increasing the azimuthal domain length L_y in the self-consistent simulations changes the behaviour of the azimuthal instabilities, with a transition from short-to-long wavelength structures occurring depending on the phase location during a BM cycle. This phenomena, localised downstream of the ion sonic point (from where the ITTI is propagating towards the cathode), is associated with a significant enhancement of the wave energy density, which in turn increases the observed anomalous force and electron transport. The local plasma parameters are strongly affected by the ITTI, which in turn impacts the growth of the azimuthal EDI modes. Hence, it seems that this mode transition towards large wavelength azimuthal structures could stem directly from the interaction between the azimuthal EDI and the axial BM and ITTI, and not from an "inverse energy cascade" as claimed by previous works [26, 25].

4. Interaction between EDI and ITTI

4.1. Impact of α_ϵ

Looking at equation 4, we can see that the modified ion-acoustic growth rate is inversely proportional to the vacuum permittivity. Hence, using a scaling factor α_ϵ is expected to reduce the growth rate and damp the EDI [16]. This scaling factor has been varied from 4 to 256 (with an azimuthal domain length $L_y = 1$ cm) and its effect on the anomalous force density is shown in figure 8. Here it is seen that the anomalous force is strongly damped when a large scaling factor is used, similar to the simulation results in [56].

Moreover, it was shown in figure 5 that the ITTI oscillations are less pronounced for low α_ϵ, and that the ITTI is stronger when the discharge current drops. These two observations suggest that the presence of the EDI may indirectly damp the ITTI. This behaviour is consistent with the hypothesis of Fernandez *et al.* [52] who found that the ITTI growth rate was inversely proportional to the electron mobility ($\gamma_{ITTI} \propto \mu_e^{-1/2}$):

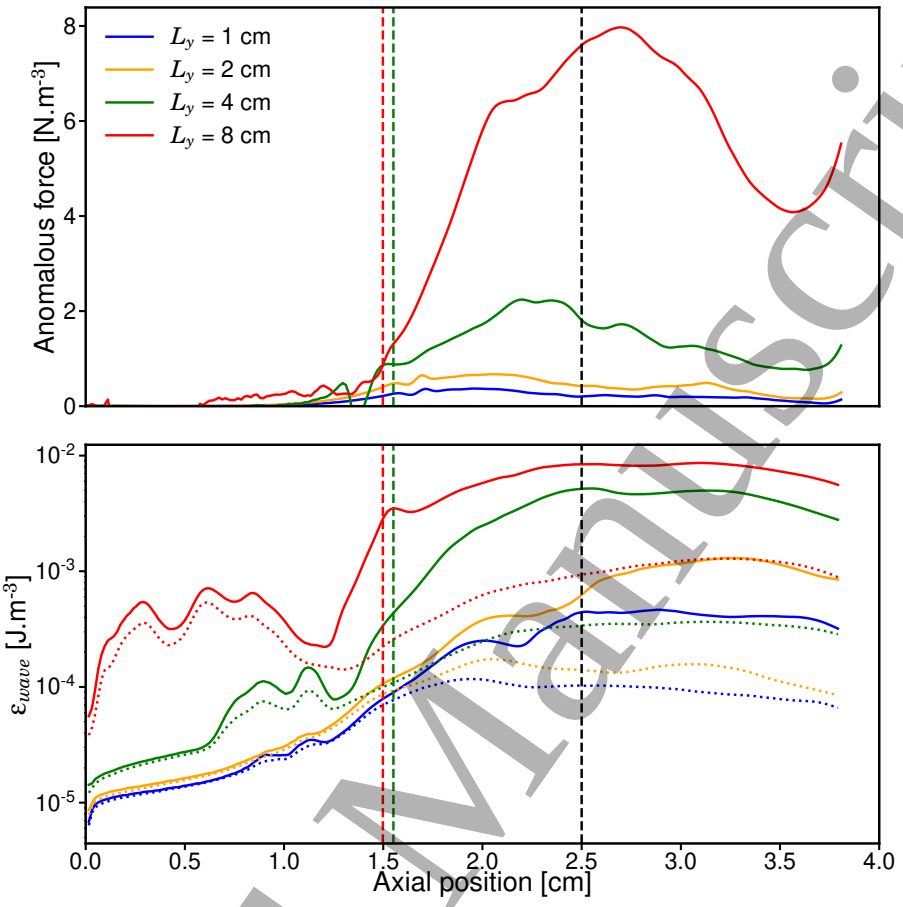

Figure 7: $\boldsymbol{\alpha_\epsilon = 64}$: Azimuthally-averaged, and time-averaged (over several BM oscillations), spatial profiles of (a) the anomalous force density, and (b) the wave energy density of the electric field obtained without a filter (plain lines) or with a high-pass filter (dotted lines). The vertical coloured dashed lines show the axial position of the ion sonic point ($v_{ix} = c_s$) for L_y=4 and 8 cm respectively. The black dashed line indicates the position of the maximum magnetic field.

hence, the high mobility at low values of α_ϵ, and during I_d growth (since the mobility is enhanced by the EDI) could be damping this ITTI. This damping of axial modes due to strong electron mobility was also recently observed by Smolyakov *et al.* [57] with both 1D fluid, and hybrid models.

4.2. Simulation case closer to reality with $\alpha_\epsilon = 4$

As the scaling factor has a strong effect on the EDI growth, simulations with a lower value of $\alpha_\epsilon = 4$ are investigated further. Because this case is the most costly in terms of computational time, it has only been run for 150 μs, and a relatively small azimuthal domain length ($L_y = 1$ cm).

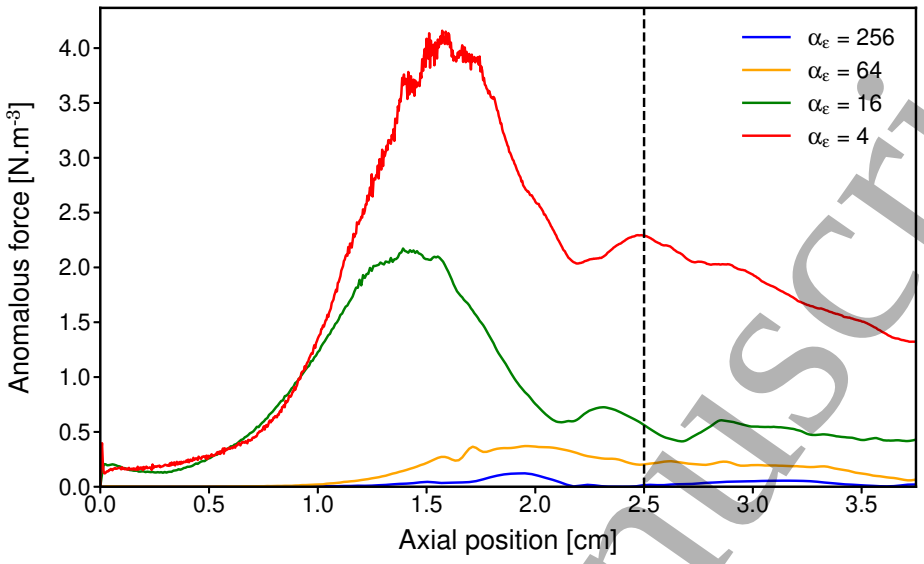

Figure 8: $\boldsymbol{L_y = 1}$ **cm**: Time-averaged (over several BM oscillations) and azimuthally-averaged, profiles of the anomalous force R_{anom} for different α_ϵ. Black dashed line: position of the maximum magnetic field.

Axial electron transport during a BM oscillation In figures 7 and 8, the time-averaged anomalous force over several BM cycles was presented. It is however interesting to investigate the impact of the BM on the axial electron transport at instantaneous moments in time. Even though the BM oscillations have an irregular shape (because of the turbulent and chaotic nature of numerous oscillatory phenomena), a representative discharge current cycle is displayed in the right-hand side inset figures of figure 9. The subsequent analysis was also performed on other BM cycles to ensure reproducibility of the results.

Similarly to the results in [56], when the discharge current increases, the anomalous force also increases, which occurs because of the increase in plasma density. When the discharge current decreases, the anomalous force begins to damp inside the thruster, but remains quite high in the plume. This significant variation of the anomalous mobility during a BM oscillation (with a maximum when the discharge current is maximum) has already been observed experimentally with laser-induced fluorescence [58]. Since the anomalous force is a major contributor to the axial electron transport [19, 56], being able to correctly describe this term is important for understanding electron transport throughout the evolution of a BM cycle. With this in mind, the kinetic model in Eq. 2 is compared with the anomalous force obtained directly from the PIC.

We observe in figures 9(a) and 9(b) that during the current rise, the theoretical derivation $R_{ei,approx}$ approximates rather well the anomalous force from the PIC. However, the fitting is not perfect (particularly for $x \geq 2$ cm) and hence, we have used the approximation $R_{ei,approx,fft}$, which makes no hypothesis on the wavenumber of the dominant azimuthal mode (which is now directly computed from an FFT). One can

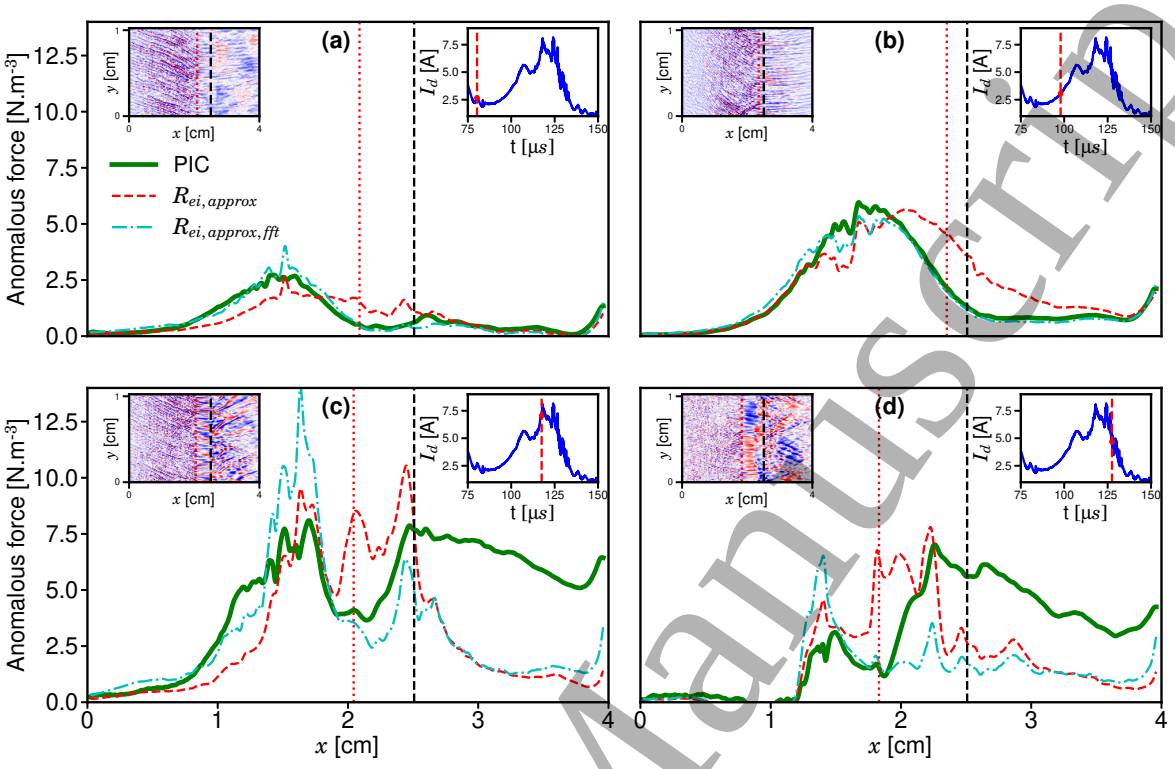

Figure 9: $\boldsymbol{\alpha_\epsilon = 4}$**,** $\boldsymbol{L_y = 1}$ **cm**: Anomalous force at different moments within a BM cycle: (a) minimum current, (b) current rise, (c) current peak and (d) current drop. The PIC results (green) are compared with the kinetic model in Eq. 2. The red vertical dotted line shows the axial position of ion sonic point ($v_{ix} = c_s$), while the vertical black dashed lines show the axial position of the maximum magnetic field. Top left inset: 2D snapshot of the azimuthal electric field at the corresponding time. Top right inset: Time evolution of discharge current, with the red dot indicating the corresponding time.

notice that a near perfect agreement with the PIC is observed. This demonstrates that during the current rise, the anomalous force is well described the kinetic model, and hence that the anomalous force is indeed an instability-enhanced electron-ion friction force produced by the EDI.

However, looking at the current drop in figures 9(c) and 9(d), it can be seen that even though fairly good agreement with PIC is obtained inside the thruster upstream of the ion sonic point, the model underestimates the anomalous force downstream. It seems then that convection of the EDI towards the cathode is not sufficient to explain the magnitude of the anomalous force in this region. Snapshots of the azimuthal electric field are displayed in left-hand side insets in figure 9, and for the decreasing current phase of the BM, we observe the presence of long-wavelength azimuthal structures that appear downstream of the ion sonic point. By looking at the time evolution of the discharge current in the right-hand side insets, it can be seen that, when these long-wavelength structures appears in figure 9(d), the discharge current oscillates with a frequency similar

to the one of the ITTI. This observation may indicate that there is interaction between the EDI and ITTI that enhances the anomalous force in this region, and this interaction may be responsible for the transition towards long-wavelength structures.

Plasma fluctuations The time evolution of the axial electric field E_x, and azimuthal electric field $< \delta E_y >$ are shown in figure 10 to try and help explain the behaviour observed above, which is not present in simulations that ignore the neutral dynamics.

Analysing the azimuthal electric field, it is seen to follow the same trend as the discharge current: the magnitude increases as the discharge current rises. However, we can distinguish three different zones, delimited by the axial location at which the ion axial velocity changes sign (green curve), and when it becomes sonic point (i.e. where $v_{ix} = c_s$; red curve). When the current rises ($t < 120$ μs), fluctuations in E_y are mostly located upstream of the ion sonic point. The wave appears to originate near the position of null axial ion drift velocity (which corresponds approximately to the zone where the plasma density is a maximum, and also where the EDI growth rate is expected to be highest) and are convected either towards the anode, or towards the cathode, with a group velocity close to the axial ion drift velocity v_{ix} [20]. They propagate azimuthally with a phase velocity close to the ion sound speed c_s: these waves are ion-acoustic in nature, as described by the EDI. Moreover, one can notice that at the ion sonic point, the waves appear to transition from oblique to purely azimuthal, as seen already in the insets of figure 9. This phenomenon was also observed in the non self-consistent simulations in Figure 1 and in almost all previous axial-azimuthal PIC simulations [19, 36, 32]. It could be related to instability convection: from the conservation equation for the wave energy density, energy convection occurs at the wave group velocity. Upstream of the ion sonic point, the group velocity is lower than the phase velocity ($v_{ix} < c_s$), so wave convection would be expected to occur obliquely. However, downstream of the sonic point, ions are rapidly accelerated by the applied electric field, and their axial drift velocity becomes much higher than the wave phase velocity ($v_{ix} \gg c_s$). Thus, wave energy is expected to be convected more strongly in the axial direction, and hence appear as a purely azimuthal wave.

However, when the ions become supersonic, the wave seems to be strongly damped during the current rise, but when the current drops ($t > 120$ μs), the fluctuations downstream of this sonic point are stronger, with no obvious axial convection. This could explain the results in figure 9: there is a change of wave behaviour at the ion sonic point. Upstream, the EDI has a modified ion-acoustic character and is then convected downstream, damping when the discharge current reaches its peak and begins to decrease. Moreover, the normalized electron density $\frac{<\delta n_e>}{n_e}$ and plasma potential fluctuations $\frac{<\delta\phi>}{T_e}$ (not shown here; see [40] for further details) show similar behaviour upstream of the sonic point, but again change in the downstream region when the discharge currents decreases. Thus, the azimuthal wave behaviour cannot be fully-described by kinetic theory.

Finally, it is interesting to look at the evolution of the axial electric field, where we

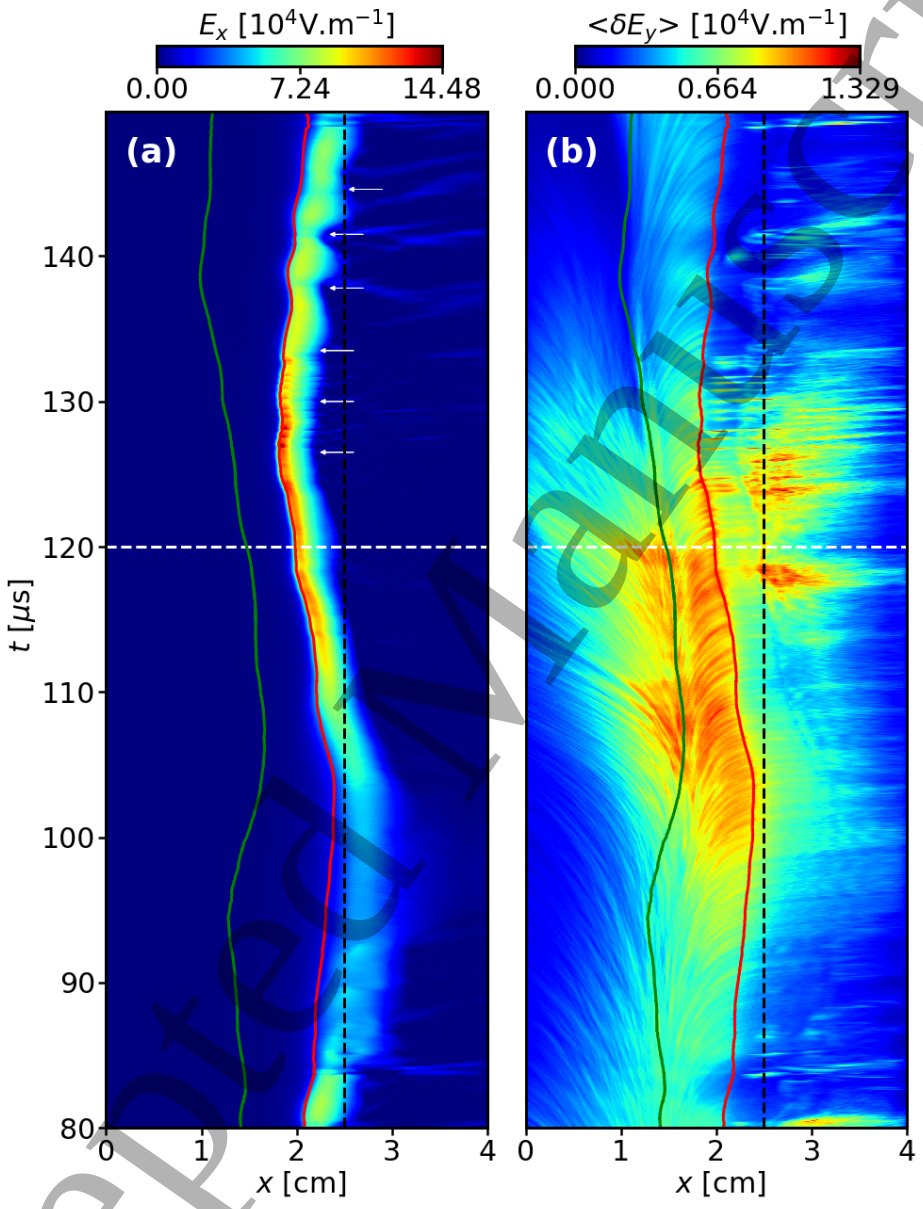

Figure 10: **$\alpha_\epsilon = 4$, $L_y = 1$ cm**: Time and axial evolution during one BM oscillation of: (a) the axial electric field, (b) the azimuthal electric field. Green vertical curve: axial position of the null ion axial velocity. Red vertical curve: axial position of ion sonic point ($v_{ix} = c_s$). Horizontal white dashed line: time when the discharge current is a maximum (t=120μs). Vertical black dashed lines: axial position of the maximum magnetic field. White arrows: indicate the troughs of axial electric field due to the ITTI.

retrieve the expected behaviour that the position of the maximum electric field oscillates axially throughout a BM cycle, moving towards the cathode when I_d increases, and towards the anode when I_d decreases. Also, we can see that downstream of the ion sonic point, on the decreasing part of the discharge current, the axial electric field oscillates with a frequency of around 300 kHz. This is the signature of the ITTI, already observed in the discharge current in the inset of figure 9. The troughs of axial electric field have been indicated by white arrows and one can notice that these oscillations are more visible when the discharge current is lower ($t > 140$ μs), as the EDI is weaker there.

4.3. A transition at the ion sonic point

Finally, to highlight the importance of the ion sonic point on the interaction between the EDI and ITTI, the Power Spectral Density (PSD) of ion density fluctuations $\delta n_i = n_i - < n_i >_y$ (with $< . >_y$ being the average over the azimuthal direction) has been computed over several breathing modes cycles, at different axial positions, for different α_ϵ (with $L_y = 1$ cm) in figure 11, and different L_y (with $\alpha_\epsilon = 64$) in figure 12. One can notice that the low-frequency peak ($f \approx 20$ kHz) corresponding to the breathing mode oscillations is present for all the simulations except the one with $\alpha_\epsilon = 4$ (in figure 11(d)) because only 150 μs have been simulated for this case.

First, we can see in figure 11 that when the scaling factor α_ϵ is decreased, the amplitude of the high-frequency peak increases and, as expected, the corresponding frequency also increases (the frequency of the dominant ion-acoustic mode is given by $\omega = \frac{\omega_{pi}}{\sqrt{3}} = \sqrt{\frac{q^2 n_e}{3\epsilon_0 M}}$). In contrast, the low-frequency content between 100 and 500 kHz has a smaller amplitude. We retrieve the previous observation that for all cases, upstream of the ion sonic point (i.e. for $x \leq 1.5$ cm), high-frequency oscillations dominate, while downstream of the ion sonic point, the low-frequency oscillations dominate. Additionally, one can notice that similarly to previous numerical works [19, 36, 24] and Thomson scattering measurements [59], no cyclotron resonances are observed in the upstream region. The absence of such resonances is likely related to non-linear resonance broadening, as first predicted by Lampe *et al.* [13]. In other experimental work [30], resonances were observed in the power spectra of ion density fluctuations and the authors explained this difference with [59] by stating that the nonlinear cascade towards long wavelength is significantly stronger for electrons compared to the ions [26] and hence, because the Thomson scattering diagnostic measures electron fluctuations, the resonances disappear in [59]. However, these results might be inconsistent with previous theoretical work [60] in which the full EDI dispersion relation was solved and it was shown that when one includes 2D or 3D effects with the radial thruster direction, then even for relatively low radial wavenumbers, these resonances are naturally smoothed over. Finally, it is difficult to give a definitive explanation for the differences with these experimental results as some limiting assumptions were used here (e.g. reduced azimuthal dimension and increased vacuum permittivity) and moreover, the thruster geometry and operating conditions were different in [30] (a bigger thruster was used):

there is no reason at present to expect that the behaviour of all Hall thrusters will be identical, and hence in some systems, resonances may be present, while in other systems they may be absent.

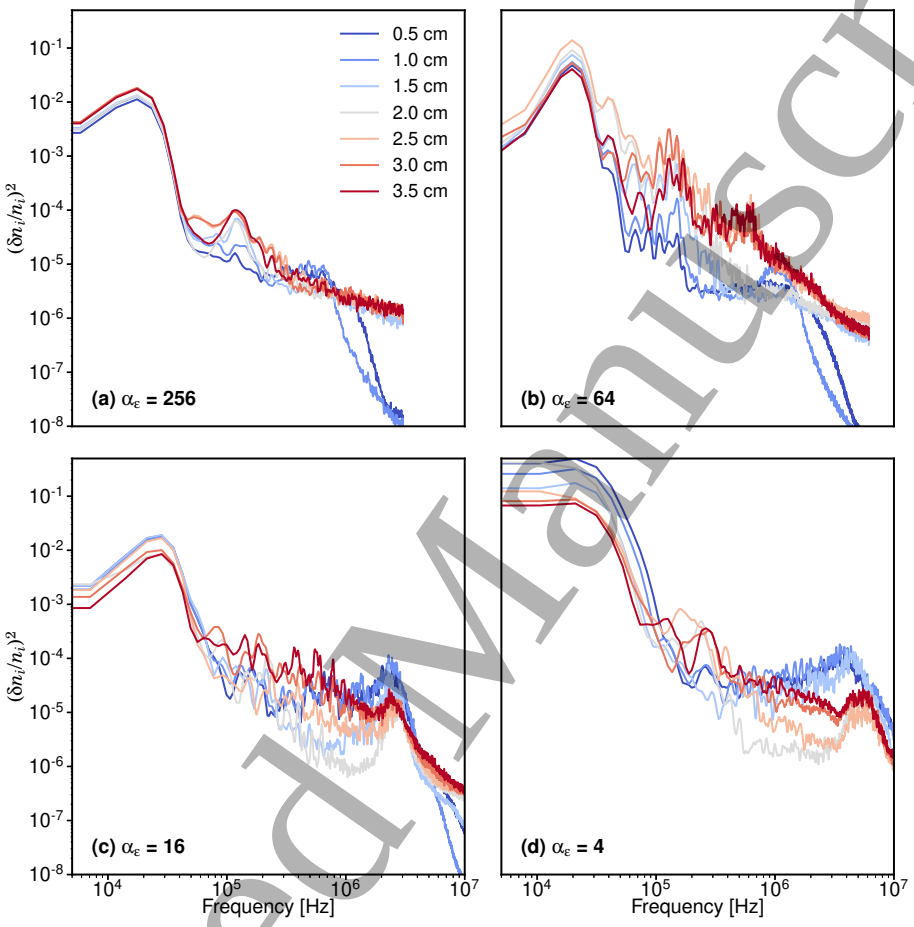

Figure 11: $\boldsymbol{L_y = 1}$ **cm**: Power Spectral Density of ion density fluctuations normalized by the averaged ion density, at different axial positions, for (a) $\alpha_\epsilon = 256$, (b) $\alpha_\epsilon = 64$, (c) $\alpha_\epsilon = 16$ and (d) $\alpha_\epsilon = 4$.

Performing the same analysis for different azimuthal lengths, we can see in figure 12 that upstream of the ion sonic point (i.e. for $x \leq 1.5$ cm), the high frequency peak is localized at the same frequency (around 1 MHz), independently of L_y. This is reassuring because it means that in this zone, the EDI is not affected by the azimuthal domain length. On the contrary, the low-frequency peak, which dominates downstream of the ion sonic point (i.e. for $x > 1.5$ cm), seems to be shifted to higher frequencies as L_y is increased. More importantly, the overall fluctuation level increases with L_y and downstream of the ion sonic point, the energy is almost completely contained in the low-frequency fluctuations (consistent with that observed in figure 7(b)).

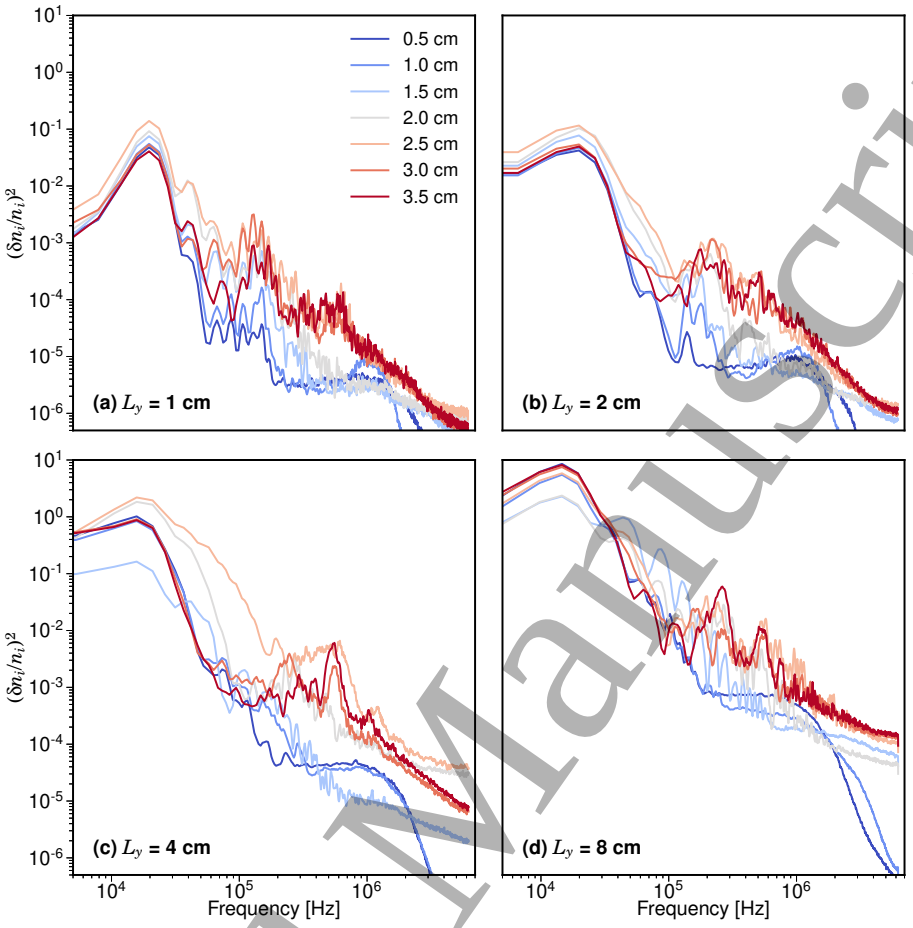

Figure 12: $\boldsymbol{\alpha_\epsilon}$**=64**: Power Spectral Density of ion density fluctuations normalized by the averaged ion density, at different axial positions, for (a) $L_y = 1$ cm, (b) $L_y = 2$ cm, (c) $L_y = 4$ cm and (d) $L_y = 8$ cm.

These two figures echo what has recently been observed experimentally by Brown and Jorns [30], with an axial transition between similar ranges of frequencies that strengthens the hypothesis that there is an interaction between the azimuthal EDI and axial ITTI which causes a mode transition towards long-wavelength structures.

5. Conclusion

In this work, we have used a 2D axial-azimuthal PIC code, which includes a 1D neutral dynamics fluid solver, to study the interaction between axial instabilities (Breathing Mode and Ion Transit-Time Instabilities) and azimuthal instabilities (Electron Drift Instability), and how this interaction affects anomalous electron transport in Hall Thrusters. First, we extended the azimuthal domain length in a steady non self-consistent simulation and observed that no long-wavelength structures or inverse cascade developed: the EDI retains a modified ion-acoustic high-frequency, short-wavelength, character. Hence, if axial instabilities are not present, electron transport can be well

described by a previously derived kinetic model [23, 24].

However, when going towards self-consistent simulations including neutral dynamics, anomalous transport was significantly enhanced for longer azimuthal domain lengths due to a mode transition from short to long-wavelength structures. This transition occurs just downstream of the ion sonic point, a location where the ITTI originates and propagates downstream in the axial direction. We have made the hypothesis that these large wavelength structures stem from an interaction between the EDI and the ITTI. Since the ITTI strongly affects the local plasma parameters, the EDI is expected to also be strongly modified. This was already observed with a 2D fluid model [25] in which axial resistive modes were found to destabilize azimuthal modes, generating large scale structures and enhancing the axial electron transport via an apparent inverse energy cascade. It would be interesting to study to what extent this fluid analysis applies to the present PIC results. In the 1D azimuthal PIC simulations of Janhunen *et al.* [26], the authors attributed the mode transition to an inverse energy cascade but several simplifying assumptions were used (no wave convection is present, no steady-state is reached and the electron temperature continually increases). More realistic 2D PIC simulations where these assumptions are removed however, do not observe any energy cascades [36, 24]. Moreover, 1D PIC simulations performed in the context of space plasmas [61] have explicitly performed tests using numerical filtering to see if inverse energy cascades occur, and the authors found that energy does not cascade down. All in all, with the hypothesis that the mode transition is due to the interaction between the ITTI and EDI, we can explain why it was not observed in previous axial-azimuthal PIC simulations [19, 36, 24] and relate it with recent experimental results [55, 30]. We should keep in mind however, that the radial direction has been neglected in the 2D simulations presented in this work, which also suffer from some limitations needed to speed-up the computations, such as a reduced azimuthal domain length and the artificially increased vacuum permittivity. More realistic (but also more demanding) 3D PIC simulations, or improved experimental diagnostics, are needed to definitively explain the origin of the mode transition.

The parametric study of azimuthal domain length was largely performed for a relatively high scaling factor of $\alpha_\epsilon = 64$, which was shown to damp the EDI. Hence, a more detailed analysis was performed on how the axial electron transport is affected by the axial BM and ITTI for a scaling factor closer to "reality" ($\alpha_\epsilon = 4$ instead of 1). We have shown that transport is enhanced when the discharge current increases due to an increased anomalous force. A similar correlation between the anomalous mobility and the breathing mode oscillation was also found experimentally [58]. It appears that this anomalous force is the main contributor to the axial electron transport, throughout the whole BM cycle. A previously developed kinetic theory successfully approximates this anomalous force during some part of the BM cycle, but underestimate the anomalous force during others: particularly when the discharge current decreases.

The nature of azimuthal waves present in the discharge varies depending on the ion sound speed location. Upstream of the ion sonic point, the plasma density is high and

the EDI is dominant: the anomalous electron transport can be well approximated by kinetic theory which identifies the anomalous force as an instability-enhanced electron-ion friction force. However, when the ions become supersonic, another instability is present and propagating axially: the ITTI. While its strength is damped when the electron mobility is high, and when the discharge current increases, it interacts with the EDI when the discharge current decreases, resulting in an enhanced anomalous transport in this region due to long-wavelength modes, which are currently not described by the kinetic model. This indicates that in any real Hall thruster, anomalous electron transport may be the result of the complex interaction between a number of different instabilities. Finally, in "real" cases with no artificial scaling, the ITTI will be damped due to a stronger EDI growth rate, hence reducing the wave energy increase observed for longer azimuthal domain lengths. As the ITTI is definitely observed experimentally in real HTs however, it will still interact with the EDI. This hypothesis requires further investigations (lower α_ϵ with longer L_y) that are very computationally expensive.

Acknowledgments

The authors would like to thank Roberto Martorelli for a number of insightful discussions. T.C., A.B. and P.C. acknowledge support from the Agence Nationale de la Recherche under the reference ANR-16-CHIN-0003-01 and Safran Aircraft Engines within the project POSEIDON. They also acknowledge access to the HPC resources of CINES (under the allocations A0060510439 and A0080510439 made by GENCI) and of CERFACS at Toulouse, and they would like to thank the HLST team of CINES for valuable help in improving the code scalability.

References

[1] Lev D, Myers R M, Lemmer K M, Kolbeck J, Koizumi H and Polzin K 2019 *Acta Astronautica* **159** 213 – 227
[2] Levchenko I, Xu S, Mazouffre S, Lev D, Pedrini D, Goebel D, Garrigues L, Taccogna F and Bazaka K 2020 *Phys. Plasmas* **27** 020601
[3] Morozov A and Savelyev V 2000 *Rev. Plasma Phys.* **21**
[4] Meezan N, Jr W H and Cappelli M 2001 *Phys. Rev. E* **63** 026410
[5] Sydorenko D, Smolyakov A, Kaganovich I and Raitses Y 2006 *Phys. Plasmas* **13** 014501
[6] Raitses Y, Kaganovich I D, Khrabrov A, Sydorenko D, Fisch N J and Smolyakov A 2011 *IEEE Trans. Plasma Sci.* **39** 995–1006
[7] Sydorenko D, Smolyakov A, Kaganovich I and Raitses Y 2008 *Phys. Plasmas* **15** 053506
[8] Taccogna F, Longo S, Capitelli M and Schneider R 2009 *Appl. Phys. Lett.* **94** 251502
[9] Ahedo E, Gallardo J M and Martinez-Sanchez M 2003 *Phys. Plasmas* **10** 3397–3409
[10] Croes V, Lafleur T, Bonaventura Z, Bourdon A and Chabert P 2017 *Plasma Sources Sci. Technol.* **26** 034001
[11] Tavant A, Croes V, Lucken R, Lafleur T, Bourdon A and Chabert P 2018 *Plasma Sources Sci. Technol.* **27** 12
[12] Forslund D W, Morse R L and Nielson C W 1970 *Phys. Rev. Lett.* **25** 1266

[13] Lampe M, Manheimer W, McBride J B and Orens J H 1972 *Phys. Fluids* **15** 2356–2362

[14] Ducrocq A 2006 *Rôle des instabilités électroniques de dérive dans le transport électronique du propulseur à effet Hall* Phd thesis Ecole polytechnique

[15] Adam J C, Heron A and Laval G 2004 *Phys. Plasmas* **11** 295–305

[16] Coche P and Garrigues L 2014 *Phys. Plasmas* **21** 023503

[17] Mikellides I, Jorns B, Katz I and Lopez Ortega A 2016 Hall2de simulations with a first-principles electron transport model based on the electron cyclotron drift instability *52nd AIAA/SAE/ASEE Joint Propulsion Conference* (American Institute of Aeronautics and Astronautics, AIAA 2016-4618)

[18] Croes V, Tavant A, Lucken R, Martorelli R, Lafleur T, Bourdon A and Chabert P 2018 *Phys. Plasmas* **25** 063522

[19] Lafleur T and Chabert P 2018 *Plasma Sources Sci. Technol.* **27** 015003

[20] Lafleur T, Baalrud S D and Chabert P 2017 *Plasma Sources Sci. Technol.* **26** 024008

[21] Lafleur T, Baalrud S D and Chabert P 2016 *Phys. Plasmas* **23** 053502

[22] Lafleur T, Baalrud S D and Chabert P 2016 *Phys. Plasmas* **23** 053503

[23] Lafleur T, Martorelli R, Chabert P and Bourdon A 2018 *Phys. Plasmas* **25** 061202

[24] Charoy T, Lafleur T, Tavant A, Chabert P and Bourdon A 2020 *Phys. Plasmas* **27** 063510

[25] Koshkarov O, Smolyakov A, Raitses Y and Kaganovich I 2019 *Phys. Rev. Lett.* **122**(18) 185001

[26] Janhunen S, Smolyakov A, Chapurin O, Sydorenko D, Kaganovich I and Raitses Y 2018 *Phys. Plasmas* **25** 011608

[27] Smolyakov A, Zintel T, Couedel L, Sydorenko D, Umnov A, Sorokina E and Marusov N 2020 *Plasma Phys. Rep.* **46** 496–505

[28] Janhunen S, Smolyakov A, Sydorenko D, Jimenez M, Kaganovich I and Raitses Y 2018 *Phys. Plasmas* **25** 082308

[29] Taccogna F, Minelli P, Asadi Z and Bogopolsky G 2019 *Plasma Sources Sci. Technol.* **28** 064002

[30] Brown Z and Jorns B 2019 *Phys. Plasmas* **26** 113504

[31] Powis A, Carlsson J, Kaganovich I, Rodriguez E, Raitses Y and Smolyakov A 2019 Scaling of spoke rotation frequency within a penning discharge and code development updates *36th International Electric Propulsion Conference,Vienna* (Paper A816)

[32] Charoy T, Boeuf J P, Bourdon A, Carlsson J A, Chabert P, Cuenot B, Eremin D, Garrigues L, Hara K, Kaganovich I D, Powis A T, Smolyakov A, Sydorenko D, Tavant A, Vermorel O and Villafana W 2019 *Plasma Sources Sci. Technol.* **28** 105010

[33] Croes V 2018 *Modélisation bidimensionnelle de la décharge plasma dans un propulseur de Hall* Ph.D. thesis Université Paris-Saclay, France

[34] Birdsall C and Langdon A 1991 *Plasma physics via computer simulation* (Institute of Physics) chap 16

[35] Coche P 2013 *Modélisation cinétique d'un propulseur à effet Hall* Ph.D. thesis Université Toulouse 3 Paul Sabatier

[36] Boeuf J P and Garrigues L 2018 *Phys. Plasmas.* **25** 061204

[37] Boccelli S, Charoy T, Alvarez Laguna A, Chabert P, Bourdon A and Magin T E 2020 *Phys. Plasmas* **27** 073506

[38] Tavant A 2019 *Plasma-wall interaction and electron transport in Hall Effect Thrusters* Ph.D. thesis Université Paris-Saclay, France

[39] Toro E F, Spruce M and Speares W 1994 *Shock Waves* **4** 25–34

[40] Charoy T 2020 *Numerical study of electron transport in Hall thrusters* Ph.D. thesis Institut polytechnique de Paris, France

[41] Kawashima R, Hara K and Komurasaki K 2017 *Plasma Sources Sci. Technol.* **27**

[42] Szabo J J 2001 *Fully Kinetic Numerical Modeling of a Plasma Thruster* Ph.D. thesis Massachusetts Institute of Technology

[43] Esipchuck Y, Morozov A I, Tilinin G N and Trofimov A V 1974 *Sov. Phys. Tech. Phys.* **18** 928

[44] Vaudolon J and Mazouffre S 2015 "investigation of the ion transit time instability in a hall

thruster combining time-resolved lif spectroscopy and analytical calculations, *Joint Conference of 30th International Symposium on Space Technology and Science, 34th International Electric Propulsion Conference and 6th Nano-Satellite Symposium* (IEPC-2015-90259/ISTS-2015-b-90259)

[45] Vaudolon J and Mazouffre S 2015 *Plasma Sources Sci. Technol.* **24** 032003

[46] Fife J M 1998 *Hybrid-PIC modeling and electrostatic probe survey of Hall thrusters* Ph.D. thesis (Massachussets Institute of Technology

[47] Hagelaar G J M, Bareilles J, Garrigues L and Boeuf J P 2003 *J. Appl. Phys.* **93** 67–75

[48] Bareilles J, Hagelaar G J M, Garrigues L, Boniface C, Boeuf J P and Gascon N 2004 *Phys. Plasmas* **11** 3035–3046

[49] Esipchuk Y and Tilinin G N 1976 *Sov. Phys. Tech. Phys.* **21** 417

[50] Barral S, Makowski K, Peradzyński Z and Dudeck M 2005 *Phys. Plasmas* **12** 073504

[51] Chable S and Rogier F 2005 *Phys. Plasmas* **12** 033504

[52] Fernandez E, Scharfe M K, Thomas C A, Gascon N and Cappelli M A 2008 *Phys. Plasmas* **15** 012102

[53] Koshkarov O, Smolyakov A I, Romadanov I V, Chapurin O, Umansky M V, Raitses Y and Kaganovich I D 2018 *Phys. Plasmas* **25** 011604

[54] https://docs.scipy.org/doc/scipy-0.14.0/reference/generated/scipy.signal.welch.html (signal.welch scipy function)

[55] Tsikata S and Minea T 2015 *Phys. Rev. Lett.* **114** 185001

[56] Charoy T, Lafleur T, Tavant A, Bourdon A and Chabert P 2019 Oscillation analysis in hall thrusters with 2d (axial-azimuthal) particle-in-cell simulations *36th International Electric Propulsion Conference,Vienna* (Paper A487)

[57] Smolyakov A, Chapurin O, Romadanov I, Raitses Y, Kaganovich I, Hagelaar G and Boeuf J 2019 Stationary profiles and axial modes oscillations in hall thrusters *AIAA Propulsion and Energy Forum, Indianapolis (AIAA 2019-4080)*

[58] Dale E T and Jorns B A 2019 *Phys. Plasmas* **26** 013516

[59] Tsikata S, Lemoine N, Pisarev V and Grésillon D M 2009 *Phys. Plasmas* **16** 033506

[60] Cavalier J, Lemoine N, Bonhomme G, Tsikata S, Honore C and Gresillon D 2013 *Phys. Plasmas* **20** 082107

[61] Muschietti L and Lembège B 2013 *J. Geophys. Res* **118** 2267–2285